

A Lossless Differential Fourier-Transform Spectrometer for precision Sunyaev-Zel'dovich effect measurements

Alessandro Schillaci¹, Giuseppe D' Alessandro¹, Paolo de Bernardis¹,
Silvia Masi¹, Camila Paiva Novaes², Massimo Gervasi³, Mario Zannoni³

¹ Dipartimento di Fisica, Università di Roma "La Sapienza", Roma, Italy

² Divisão de Astrofísica, Instituto Nacional de Pesquisas Espaciais, São José dos Campos, SP, Brazil

³ Dipartimento di Fisica G. Occhialini, Università Milano Bicocca, Milano, Italy

Submitted: Jan. 12th, 2014 ; Accepted: ...th, 2014

ABSTRACT

Context. Precision measurements of the Sunyaev-Zel'dovich Effect (SZE) in clusters of galaxies require excellent rejection of common-mode signals and wide frequency coverage.

Aims. We describe an imaging, lossless, differential Fourier Transform Spectrometer (FTS), optimized for measurements of faint brightness gradients at millimeter wavelengths.

Methods. Our instrument is based on a Martin-Puplett Interferometer (MPI) configuration. We combine two MPIs working synchronously, in order to use the whole input power. In our implementation the observed sky field is divided in two halves along the meridian, and each half field corresponds to one of the two input ports of the MPI. In this way each detector in the FTS focal planes measures the difference in brightness between two sky pixels, symmetrically located with respect to the meridian. Exploiting the high common-mode rejection of the MPI we can measure small sky brightness gradients over a large isotropic background.

Results. The instrument works in the range $\sim 1 \div 20 \text{ cm}^{-1}$ ($30 \div 600 \text{ GHz}$), has a maximum spectral resolution $1/(2 \text{ OPD}) = 0.063 \text{ cm}^{-1}$ (1.9 GHz), and an unvignetted throughput of $2.3 \text{ cm}^2 \text{ sr}$. It occupies a volume of $0.7 \times 0.7 \times 0.33 \text{ m}^3$ and has a weight of 70 kg. This design can be implemented as a cryogenic unit to be used in space, as well as a room-temperature unit working at the focus of sub-orbital and ground based mm-wave telescopes. The first in-flight test of the instrument is with the OLIMPO experiment on a stratospheric balloon; a larger implementation is being prepared for the Sardinia Radio Telescope.

Key words. Cosmic Microwave Background – Clusters of galaxies – Spectroscopy

1. Introduction

About 1% of the photons of the Cosmic Microwave Background (CMB) crossing a rich cluster of galaxies undergo inverse Compton scattering against the hot electrons of the intracluster plasma. This phenomenon is called the thermal Sunyaev-Zel'dovich effect (SZE), and is a powerful tool for astrophysical and cosmological investigation (Sunyaev and Zeldovich 1970, (Sunyaev and Zeldovich 1972, Rephaeli 1995, Birkinshaw 1999, Carlstrom et al. 2002).

Most of the power of the thermal SZE is due to its very characteristic spectrum: in the direction of a cluster of galaxies, the SZE induces a *decrease* of the brightness of the CMB at frequencies below 217 GHz, and an *increase* of the brightness of the CMB at frequencies above 217 GHz. In the non relativistic limit, the spectrum of the SZE can be computed from the Kompaneets equation (Kompaneets 1957) and depends only on the Comptonization Parameter y :

$$y = \int n_e \sigma_T \frac{k_B T_e}{m_e c^2} d\ell \quad (1)$$

where the integral is along the line of sight. Using the y parameter, the brightness variation ΔI_t with respect to the average cosmic microwave brightness I can be expressed as:

$$\frac{\Delta I_t}{I} = y \frac{x^4 e^x}{(e^x - 1)^2} [x \cdot \coth(x/2) - 4] \quad (2)$$

Send offprint requests to: alessandro.schillaci@roma1.infn.it

Typical values of y are $10^{-4} \div 10^{-5}$, so the SZE signal ΔI_t is very small compared to the average brightness I of the CMB. However, the SZE spectrum does not depend on the distance (redshift) of the cluster of galaxies, so clusters become important cosmological probes. Moreover, the SZE spectrum depends linearly on both the temperature and density of the intra-cluster plasma. Information from the SZE significantly complements information obtained from X-ray brightness (proportional to the density squared), to investigate the physics of the clusters. The thermal SZE is only the most evident interaction between the CMB and the plasma of the cluster. The peculiar motion of the cluster induces the kinematic SZE, and the non-thermal component of the plasma produces additional distortions (Wright 1979).

SZE measurements have recently reached maturity with the surveys of large, dedicated ground-based telescopes (see e.g. Reichardt et al. 2013, Hasselfield et al. 2013 and references therein) at low frequencies, and with the space-based survey of the Planck satellite (see Planck collaboration 2013 and references therein), covering the whole spectral range where the SZE is present.

All these are multi-band photometric measurements. The number of independent bands useful to this purpose is limited to a few for ground based observations, and was $6 \div 7$ in the case of the Planck satellite. The number of parameters describing the cluster and the foregrounds can be larger than 7: in principle

more bands and/or complementary observations in other spectral regions are needed.

Spectroscopic measurements can help very much in this situation. These allow to extract the small SZE signal even in the presence of important foreground emission, and to estimate the parameters of the cluster, removing the degeneracy present in the case of photometric measurements (see de Bernardis *et al.* 2012 and section 2 for a specific discussion).

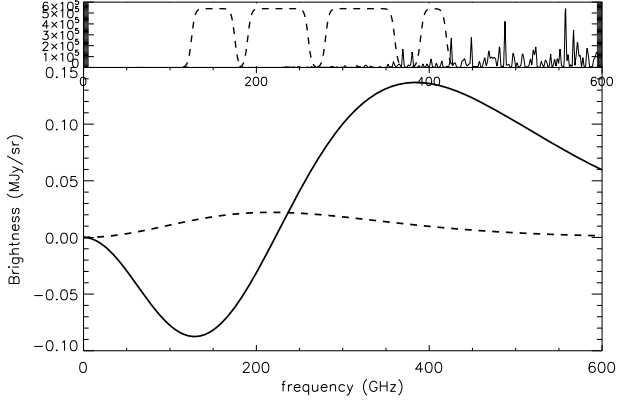


Fig. 1. Bottom: Thermal (continuous line) and kinematic (dashed line) SZE for $y = 5 \times 10^{-4}$, $v_p = 1000 \text{ km/s}$ and $T_e = 8.2 \text{ keV}$, in MJy/sr. **Top:** residual atmospheric emission at stratospheric balloon altitude (continuous line, in MJy/sr as well). Four sub-bands (see text) suitable for balloon-borne observations of the SZE are also plotted in the same panel (dashed lines).

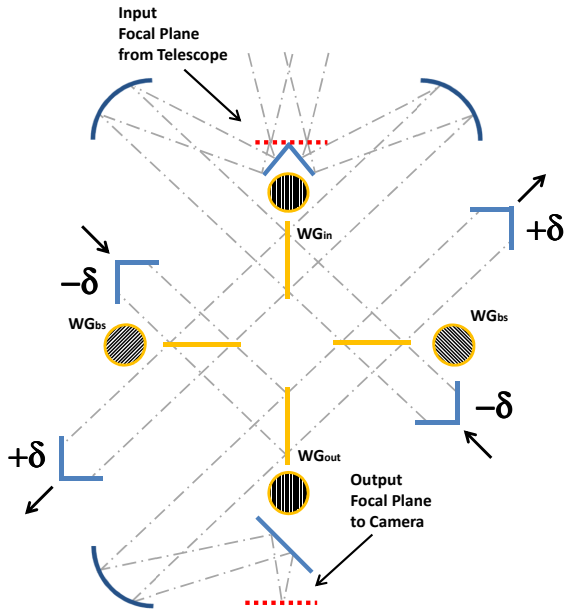


Fig. 2. Block diagram of the lossless differential MPI.

Here we present an instrument optimized for spectroscopic measurements of the SZE. Due to the continuous nature of the spectrum (see Fig. 1), high spectral resolution is not a design-driver. A coarse spectral resolution ($\sim 0.5 \text{ cm}^{-1}$) is more than enough to provide a sufficient number of independent spectral

data. Better resolution could be useful to assess the presence of contamination from molecular lines, but this is important only for low galactic latitudes. Instead, the instrument is required to be imaging (feeding a detectors array in its focal plane), to have a wide frequency coverage (almost two decades at mm/submm wavelengths) and to be differential, i.e. to measure the difference in brightness between the cluster direction and the surrounding directions, rejecting the bright isotropic background from the CMB. The class of the FTSs, and in particular the MPI (Martin and Puplett 1970), fulfills all these requirements.

The disadvantage of the FTSs is that all the frequencies from the whole frequency range to be measured contribute to form the radiative background on the detector. As a result, radiation noise is higher than in the case of dispersion spectrometers, where spectral bins are focused on the detector one at a time, sequentially.

A good tradeoff can be obtained in two ways.

First, the instrument should operate from a space-based platform (stratospheric balloon or satellite) so that only the natural (astrophysical) radiative background and the emission of the instrument are present. This is needed anyway, at least at frequencies outside the mm atmospheric windows and above 250 GHz, where atmospheric transmission is poor and atmospheric fluctuations severely limit SZE observations.

Second, the radiative background is further reduced by splitting the frequency coverage in a few sub-bands, using dichroic filters, and using one array for each sub-band (see e.g. de Bernardis *et al.* 2010). In this way the high background at the high-end of the explored frequency range does not limit the performance of the detector array measuring the low-end. In Fig. 1 we plot a sample splitting of the $0\div 20 \text{ cm}^{-1}$ range into four sub-bands optimized for observations of the SZE with reduced radiative background at balloon altitude. Wider bands, with an increased coverage can be used for space missions, where the atmospheric background is not present. In that case, a cryogenic implementation of the instrument is needed to fully exploit the reduced natural (astrophysical) background. Ground-based operation at the best sites are restricted to the 90GHz and 140GHz windows, due to the high radiative background.

In Table 1 we report the typical radiative background due to the room-temperature emissivity of mirrors (Bock *et al.* 1995) and wire-grids in the spectrometer (Schillaci *et al.* 2013), to the natural astrophysical background, and to residual atmosphere, for both a room-temperature implementation of the instrument on a good ground-based site and aboard of a balloon payload, and a cryogenic implementation aboard of a satellite.

Noticeable implementations of differential FTSs for astrophysics and cosmology are the FIRAS aboard of the COBE satellite (Mather *et al.* 1990, Fixsen *et al.* 1994) and the SPIRE-FTS aboard of the Herschel satellite (Griffin *et al.* 2010). In both cases, the brightness of the sky is compared to the brightness produced by an internal blackbody reference.

In our instrument, instead, the two input ports collect radiation from two independent sky fields, so that each detector in the focal plane of the spectrometer measures the brightness difference between two independent sky pixels. In this way the common mode signal from the instrument, the residual atmosphere, the isotropic CMB component, is rejected, and only brightness gradients are measured. For this reason we will use the acronym DFTS (Differential Fourier Transform Spectrometer) for our instrument.

In practice (see Fig. 2) the first component of our spectrometer is a wedge mirror placed in the focal plane of the telescope, which has an alt-az mount. The wedge is aligned to the elevation

Table 1. Radiative background and photon noise from instrument, atmosphere, and astrophysical background, in several sub-bands suitable for SZE measurements. Photon noise per spectral bin is computed assuming that noise from all the frequencies within the sub-band is contributing to the measurement of the considered bin. Top: room-temperature spectrometer on a ground based telescope (1mm PWV); Middle: room-temperature spectrometer on a stratospheric balloon; Bottom: cold (2K) spectrometer on a satellite. All instruments are diffraction limited at the lowest end of each sub-band. Turbulence and atmospheric fluctuations, which can be relevant in the ground-based case, are not included.

ground		
band (GHz)	background (pW)	noise in 1s (fW/GHz)
85÷110	40	55
125÷175	110	110
stratospheric balloon		
band (GHz)	background (pW)	noise in 1s (fW/GHz)
125÷175	80	90
190÷260	110	130
280÷360	110	160
390÷420	40	100
satellite		
band (GHz)	background (pW)	noise in 1s (fW/GHz)
100÷180	7	30
180÷350	10	50
350÷700	16	80
700÷1000	7	70

direction. In this way radiation from the left half of the focal plane is reflected into input port 1 of the DFTS, and radiation from the right half of the focal plane is reflected into input port 2 of the DFTS. This effectively divides the telescope field of view in two halves. In the case of SZE observations one of the two half-fields is centered on the galaxy cluster, and the other is centered on a neighboring reference region.

Once the constant common mode signal is removed from the interferogram, each detector in the focal plane of the spectrometer measures the brightness *difference* between two independent sky pixels symmetrically placed with respect to the elevation direction through the boresight. The center of the target field is compared to the center of the reference field; a pixel east of the center of the target field is compared to a pixel west of the center of the reference field; a pixel west of the center of the target field is compared to a pixel east of the center of the reference field, and so on.

In this paper we describe the implementation of a lossless DFTS for SZE in the mm/submm region. The first light of the instrument will be on a stratospheric balloon flight of the OLIMPO experiment (Masi *et al.* 2003); additional configurations have been studied for the SAGACE satellite proposal (de Bernardis *et al.* 2010), for the Millimetron satellite mission (Smirnov *et al.* 2012), and for the Sardinia Radio Telescope (Grueff *et al.* 2004).

In a classical MPI design, at the first wire grid (input polarizer) 50% of the beam intensity is lost, and doesn't reach the detectors. In our DFTS this radiation is processed by a second, identical MPI, so the instrument consists of two MPIs working simultaneously, as shown in Fig. 2, doubling the efficiency.

The paper is organized as follows: in section 2 we show that adding spectral measurements of the SZE to photometric measurements results in a significant enhancement of the ability to separate degenerate parameters describing the SZE and foreground contamination. In section 3 we describe quantitatively the operation of the DFTS and demonstrate its efficiency. In section 4 we describe the optical design strategy for the instrument. In section 5 we describe the optical optimization and the optomechanical design. Then (section 6) we discuss the most critical issues related to this configuration. In section 7 we describe the test and commissioning of the instrument. We conclude in section 8.

2. SZE Photometry and SZE Spectrometry

The number of parameters describing the SZE signal from a cluster of galaxies and the foreground emission along the same line of sight cannot be limited to a few. The optical depth τ_T and the temperature T_e of the plasma provide a good description of the thermal SZE. But other parameters must be considered. The cluster velocity component along the line of sight v_{LOS} , produces the kinematic SZE, and includes any intrinsic CMB anisotropy in the same direction (the sum of the two effects can be described by a single parameter ΔT_{CMB}). A minimum of 3 parameters describing the non-thermal population of electrons in the cluster plasma, which is responsible for the non-thermal SZE: these are its optical depth τ_{nt} , the spectral index of the power-law spectrum of the energy of the electrons α , and their minimum momentum p_1 . A minimum of 3 parameters is needed to describe the emission of interstellar dust along the line of sight, in our galaxy and in the cluster. In fact this can be minimally modelled as a thermal spectrum with optical depth τ_D , temperature T_D , and spectral index of emissivity β . Also, free-free and synchrotron emission from the diffuse medium in our Galaxy and in the galaxies in the cluster must be accounted for, and least using one amplitude parameter for each of them (ΔI_{ff} , ΔI_{sy}).

Given this situation, it is evident that few-bands photometry cannot be sufficient to constrain all these independent parameters, and even to separate the contribution due to the thermal SZE from the others. The approach of current experiments is to use heterogeneous ancillary measurements (X-ray surveys, Far IR surveys, optical surveys) to estimate several of the parameters. A direct measurement would certainly be less prone to systematic effects.

As discussed in de Bernardis *et al.* (2012), low-resolution spectroscopy of the SZE can improve significantly the situation, providing a sufficient number of degrees of freedom to fit several of the parameters above. The price to pay for spectroscopic measurements is that the sensitivity of the measurement is reduced with respect to photometric measurements taken in the same conditions. This is especially true in the case of FTSS, where radiation from the whole measured frequency range is continuously detected during the scan of the interferogram.

Here we show that combining multi-band photometric measurements and spectroscopic measurements obtained adding a DFTS in front of the same photometer is a very effective approach. In practice, photometric measurements provide high S/N ratio broad-band measurements of the SZE, while spectroscopic measurements provide the required additional degrees of freedom to distinguish the parameters to be measured.

To investigate this, we have reproduced the analysis in de Bernardis *et al.* (2012) assuming to perform spectroscopic measurements for half of the observation time, and photometric measurements in the same bands for the rest of the observation time.

Table 2. Cluster and foreground parameters estimated from simulated observations of the SZE along a line of sight towards a cluster of galaxies, using the same bands as in Fig. 1. S refers to spectroscopic observations (4 hours), S+P refers to spectroscopic observations for 4 hours, and photometric observations for 4 additional hours.

5 parameters	input	best fit (S)	best fit (S+P)
$100\tau_T$	1.70	1.76 ± 0.32	1.76 ± 0.29
kT_e (keV)	9.5	9.5 ± 1.7	9.6 ± 1.7
$10^6\tau_D$	1.85	1.85 ± 0.22	1.85 ± 0.17
$10^4\Delta T_{CMB}$	3.1	3.04 ± 1.26	3.07 ± 0.11
$10^4\tau_{nt}$	1.0	0.95 ± 2.13	1.00 ± 0.11
χ^2/DOF	-	35.8/36	39.4/40
6 parameters	input	best fit (S)	best fit (S+P)
$100\tau_T$	1.70	1.78 ± 0.42	1.74 ± 0.29
kT_e (keV)	9.5	9.6 ± 1.8	9.6 ± 1.6
$10^6\tau_D$	1.85	1.94 ± 0.13	1.82 ± 0.23
$10^4\Delta T_{CMB}$	3.1	3.07 ± 1.54	3.05 ± 0.11
$10^4\tau_{nt}$	1.0	0.38 ± 6.07	0.88 ± 0.86
p	1.0	5 ± 26	3.2 ± 6.1
χ^2/DOF	-	35.8/35	42.1/39

We have simulated the measured signals assuming that in both cases the measurements are limited by the noise of the background photons, and we have carried out a fit to the simulated data with the sum of emission from all the sources along the line of sight, described by the parameters listed above. To estimate the best fit, we have minimized the χ^2 obtained adding the χ^2 of the spectroscopic measurements and the χ^2 of the photometric measurements. The results of this procedure are summarized in Table 2 for the case of a 4-bands photometer and spectrometer with bands similar to the ones of Fig. 1. As a photometer alone, the instrument cannot measure more than 4 parameters (or independent combinations). In Table 2 we demonstrate the power of using the instrument as a spectrometer and as a spectrometer and photometer : 5 or 6 parameters can be measured, with improved performance in the case of combined measurements. This demonstrates the synergy of photometric and spectroscopic observations. As described below, our instrument is implemented so that both spectroscopic and photometric observations can be performed in sequence.

In Fig. 3 we compare data and best fit in the case of the observation simulated in Table 2, which correspond to 4 hours of integration on a typical cluster with the OLIMPO experiment.

3. The lossless differential MPI

All our implementations of the spectrometer share the same optical configuration sketched in Fig. 2: a wedge mirror splits the telescope focal plane in two halves, as described above, and two collimators redirect the two beams on opposite sides of the input polarizer WG_{IN} . This device is the input polarizer for two MPIs, one for the radiation reflected and one for the radiation transmitted. The two MPIs also share the output polarizer WG_{OUT} and the detector arrays, while the beamsplitter polarizers ($WG_{BS,L}$ and $WG_{BS,R}$) and the delay lines (δ) with the roof mirrors are replicated. Metallic wire grid polarizers are used, which provide excellent efficiency over the wide frequency range of interest.

Here we use Jones calculus to demonstrate that our optical configuration is efficient. In this formalism and following the sketch on Fig. 2 we can write the electrical fields for the two orthogonal polarizations coming from the two sources A and B

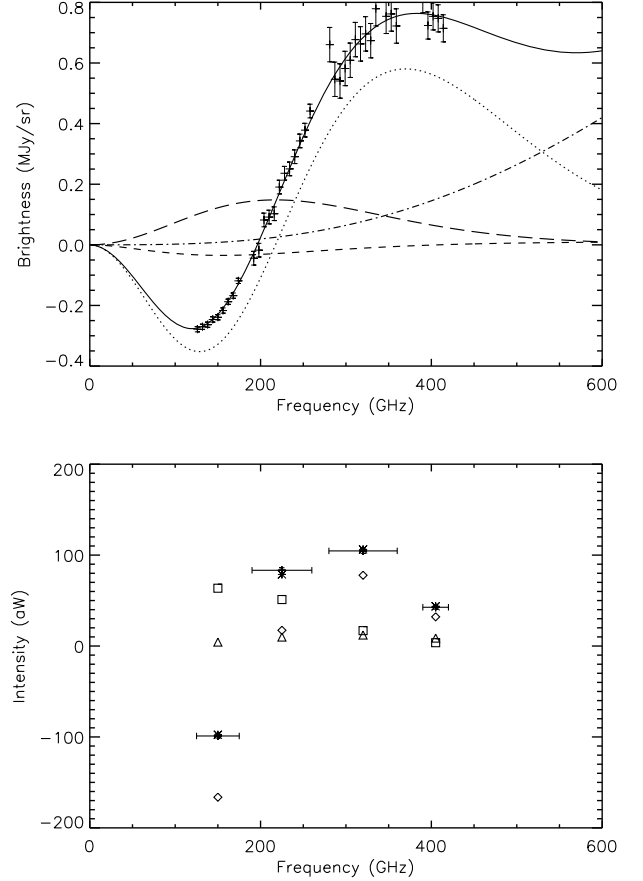


Fig. 3. Simulated spectroscopic (top) and photometric (bottom) measurements of the SZE towards the center of a typical cluster of galaxies (see Table 2 for the parameters of the cluster). The lines in the top panel represent simulated spectra of thermal SZE (dotted line), kinematic SZE + CMB anisotropy (long dashes line), non-thermal SZE (short dashes line), interstellar dust (dot-dashed line), and the best fit to the simulated data using the sum of all the components (continuous line). The data points with their error bars are computed from the sample observation described in the text, for a single bolometer of the array observing the center of the cluster. The integration time for spectroscopic measurements is 4 hours. In the lower panel, different symbols refer to the contribution to the in-band power from thermal SZE (diamonds), kinematic SZE (open squares), interstellar dust (triangles), CMB anisotropy and kinematic SZE (squares) and the best fit (asterisks). The horizontal bars refer to the FWHM bandwidth and the vertical bars are the estimate of the error for an integration time of 4 hours. The detectors are diffraction limited at the low frequency edge of the band.

as:

$$A = \begin{pmatrix} A_x \\ A_y \end{pmatrix}; B = \begin{pmatrix} B_x \\ B_y \end{pmatrix}$$

Here the reference system is right-handed and co-moving, following the propagation of the electromagnetic wave, with the z axis anti-parallel to the wavevector \mathbf{k} , and the x axis in the plane of the drawing in Fig. 2.

The matrix describing a polarizer is :

$$T_\theta = \begin{pmatrix} \cos^2(\theta) & \cos(\theta)\sin(\theta) \\ \cos(\theta)\sin(\theta) & \sin^2(\theta) \end{pmatrix}$$

when the polarizer transmits radiation and

$$R_\theta = \begin{pmatrix} \sin^2(\theta) & -\cos(\theta)\sin(\theta) \\ \cos(\theta)\sin(\theta) & -\cos^2(\theta) \end{pmatrix}$$

when reflects radiation.

Here θ is the angle between the principal axis of the polarizer and the y direction (orthogonal to the plane of the drawing in Fig. 2, and projected in the xy plane). The matrix for the ideal roof-mirror (sequencing two metal reflections) is the Identity Matrix \mathcal{I} .

The phase shift δ introduced by the optical path difference and common to both polarizations is described by the matrix

$$\Delta_\delta = \begin{pmatrix} e^{i\delta} & 0 \\ 0 & e^{i\delta} \end{pmatrix}$$

where δ is $4\pi x\sigma$, with x the mechanical path difference in the case of a single moving mirror, and σ the wavenumber (in cm^{-1}). In our implementation of the spectrometer, both delay lines have moving mirrors (moving in opposite directions), so we gain a factor two in the introduced phase-shift for a given mechanical displacement of each mirror.

Following Fig. 2, radiation from source A is processed by the left FTS after being transmitted by the input wire grid. The processed wave at the left detector array can be written as the sum of the contributions of two beams, travelling in the two arms of the left FTS:

$$E_{IA} = R_0 \cdot T_{45} \cdot \Delta_\delta \cdot \mathcal{I} \cdot R_{-45} \cdot T_0 \cdot A + R_0 \cdot R_{45} \cdot \Delta_{-\delta} \cdot \mathcal{I} \cdot T_{-45} \cdot T_0 \cdot A \quad (3)$$

Analogously we find, for the radiation of source B processed by the left FTS:

$$E_{IB} = R_0 \cdot T_{45} \cdot \Delta_\delta \cdot \mathcal{I} \cdot R_{-45} \cdot R_0 \cdot B + R_0 \cdot R_{45} \cdot \Delta_{-\delta} \cdot \mathcal{I} \cdot T_{-45} \cdot R_0 \cdot B \quad (4)$$

After simple algebra we get :

$$\begin{pmatrix} E_{Ix} \\ E_{Iy} \end{pmatrix} = \begin{pmatrix} 0 \\ B_y \cos(\delta) + iA_x \sin(\delta) \end{pmatrix}$$

For the right FTS equations (3) and (4) become:

$$E_{IIA} = T_0 \cdot T_{-45} \cdot \Delta_{-\delta} \cdot \mathcal{I} \cdot R_{45} \cdot R_0 \cdot A + T_0 \cdot R_{-45} \cdot \Delta_\delta \cdot \mathcal{I} \cdot T_{45} \cdot R_0 \cdot A \quad (5)$$

$$E_{IIB} = T_0 \cdot T_{-45} \cdot \Delta_{-\delta} \cdot \mathcal{I} \cdot R_{45} \cdot T_0 \cdot B + T_0 \cdot R_{-45} \cdot \Delta_\delta \cdot \mathcal{I} \cdot T_{45} \cdot T_0 \cdot B \quad (6)$$

So for the right FTS:

$$\begin{pmatrix} E_{IIx} \\ E_{IIy} \end{pmatrix} = \begin{pmatrix} B_x \cos(\delta) + iA_y \sin(\delta) \\ 0 \end{pmatrix}$$

The output signal detected by the left-side detector is the sum of the signals from the two MPIs:

$$\begin{pmatrix} E_x \\ E_y \end{pmatrix} = \begin{pmatrix} B_x \cos(\delta) + iA_y \sin(\delta) \\ B_y \cos(\delta) + iA_x \sin(\delta) \end{pmatrix}$$

So for the intensity:

$$I_L = |E_x|^2 + |E_y|^2$$

$$I_L = \frac{1}{2}(I_a + I_b) + \frac{1}{2}(I_a - I_b) \cos(\delta) \quad (7)$$

where the common mode and the modulated terms in the interferogram can easily be recognized. This is twice the intensity detected in a standard MPI (see e.g. Carli and Mencaraglia 1981a, 1981b). A complementary expression is found for the right-side detector array:

$$I_R = \frac{1}{2}(I_a + I_b) - \frac{1}{2}(I_a - I_b) \cos(\delta) \quad (8)$$

4. Optical design

Observations of clusters of galaxies require an angular resolution $\theta \sim 1'$. At the center frequency of the range of interest here (350 GHz) the size of the entrance pupil of the telescope should be $D \simeq 1.22\lambda/\theta \simeq 3.5m$. A detector array should be placed in the focal plane of the telescope for fast mapping, covering the entire field of view of the instrument. This should be $\Theta \sim 15'$ wide to get complete images of the cluster and of the surrounding reference areas. In order to limit the physical size of the detector array, which has to be cooled inside a cryostat for high sensitivity, the output focal ratio $f_\#$ of the telescope should not be too slow. Assuming a diameter of the detector array $d \sim 50mm$ we get a focal length $F = d/\theta \simeq 11.5m$, so that $f_\# = F/D \sim 3.3$. This will be the entrance $f_\#$ for our spectrometer, which is to be inserted between the focal plane of the telescope and the detectors array.

In Fig. 4 we show the path of the radiation inside the spectrometer from two points of view: in the upper diagram we show the path of rays coming from the sky, while in the bottom diagram we show the path of rays coming from the aperture pupil. In this sketch collimators are represented by lenses for simplicity.

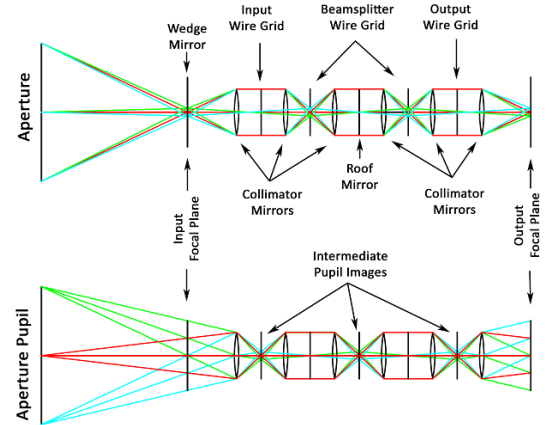


Fig. 4. Propagation of rays in the spectrometer. Top: rays coming from the sky. Bottom: rays coming from the aperture pupil.

Following the upper diagram, the feed optics (the telescope) focuses the image of the sky at the entrance of the FTS. This, in turn, produces an exit beam with the same $f_\#$. In this way the FTS can be removed, to go back to photometric measurements.

In the spectrometer we need to control the divergency of the beam, which is directly related to the dimensions of the optical components.

Also, when we move the roof mirrors to change the optical path difference, the optical configuration can change. To mitigate this problem we need to keep the beam collimated at the level of the roof mirrors. For this reason we need two intermediate focalizations in correspondence of the two beamsplitting wire grids (WG_{BS}).

In the bottom diagram of Fig. 4 we show the positions of the intermediate images of the aperture pupil (the telescope aperture): these correspond to positions where the rays from the sky are collimated. This optical scheme requires three intermediate images: two at the WG_{IN} and WG_{OUT} and a third one at the movable roof mirror. In this way, when moving the mirror, the effect of optical pickup or modulation is minimized.

The considerations above have driven the optical design of the instrument.

5. Opto-mechanical implementation

5.1. Optics optimization

The initial optical design of the lossless DFTS has been developed using ZEMAX in *Sequential Mode*. We have modeled the optical system feeding the spectrometer as a classical Cassengrain telescope, feeding a focal plane 50mm in diameter, with a focal ratio $f/3.3$. We need to insert the input ports of our DFTS in this beam, between the rear side of the primary mirror and the telescope focal plane, and produce an identical beam at the exit, so that the insertion of the DFTS does not require any change in the detector system. In this way the telescope can carry out photometric measurements when the DFTS is excluded from the system, and spectroscopic measurements when the DFTS is included. The optical recipe for the optimized system is reported in table 3. In the following we describe the optimization process for the different sections of the instrument.

Table 3. Optical Recipe for the DFTS

Name	Surface Type	Aperture Type	Dimension ϕ (mm)	Radius 1 (mm)	Conic 1	Radius 2 (mm)	Conic 2	Decenter [X,Y] (mm)
Folder Mirror (front)	Plane	Elliptical	170 x 210	0	0	0	0	[0,14]
Wedge (half)	Plane	Rectangular	40 x 40	0	0	0	0	[20,0]
Collimator I	Biconic	Circular	140	-590.784	-0.870	-588.797	-0.678	[-90,82]
Wire Grid IN	Plane	Circular	110	0	0	0	0	[0,0]
Collimator II	Biconic	Circular	130	-543.402	-0.781	-514.178	-1.108	[288,0]
Wire Grid BS	Plane	Circular	50	0	0	0	0	[0,0]
Collimator RM	Parabolic	Circular	90	-300.159	-1	0	0	[-168,0]
Roof Mirror (half)	Plane	Rectangular	58 x 80	0	0	0	0	[29,0]
Collimator III	Biconic	Circular	176	-543.402	-0.781	-514.178	-1.108	[-288,0]
Wire Grid OUT	Plane	Circular	160	0	0	0	0	[0,0]
Collimator OUT	Biconic	Circular	130	-8047.496	-2.202	-6883.036	-3.245	[-1272,1162]
Plane Mirror	Plane	Elliptical	90 x 55	0	0	0	0	[0,0]
Folder Mirror (back)	Plane	Elliptical	170 x 210	0	0	0	0	[0,14]
Lens	Plano-Convex	Circular	120	163.938	-1.478	0	0	[0,0]

5.2. Input section

Radiation coming from the Cassengrain secondary mirror is deflected towards the input port of the DFTS by a flat folding mirror at 45° . To better fit the available room between the rear side of the primary mirror of the telescope and the cryostat of the detectors, the optical system of the DFTS is developed in a plane orthogonal to the optical axis of the telescope (see Fig. 7).

The input section of the DFTS is shown in Fig. 6. In the location of the deflected focal plane we place our *image divider*. A

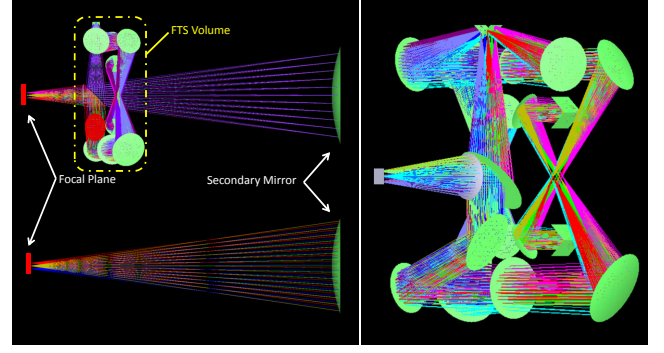


Fig. 5. Right: General ray-tracing in the interferometer. Left: location of the interferometer between the secondary mirror and the focal plane inside the cryostat (top); ray tracing with the interferometer excluded (bottom).

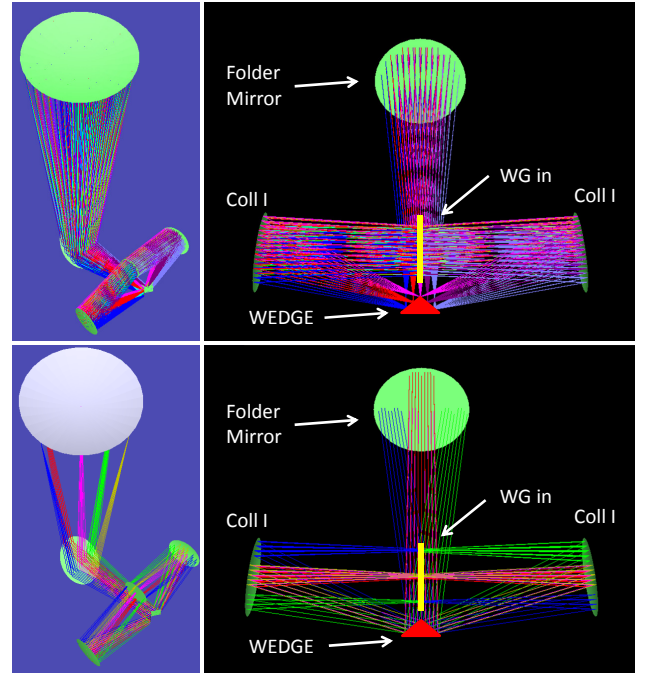


Fig. 6. The input section of the DFTS. Top: rays from the sky. Bottom: rays from the secondary mirror of the telescope.

wedge mirror, with vertex in the focal plane, splits the image of the sky in two halves (see Fig. 6). The two halves are reflected towards two independent collimators ($Coll_I$), symmetrically located with respect to the focal plane.

The two sides of the mirror are $40\text{mm} \times 40\text{mm}$ and they are tilted $\pm 36^\circ$ with respect to the optical axis. The two $Coll_I$ have a *Biconic* surface, optimized to reproduce the aperture pupil at the input wire grid WG_{IN} position.

Hereafter we will consider the center of the field of view of the single half of the wedge as our optical axis. On WG_{IN} we have the image of the secondary mirror of the telescope that is the aperture stop of the optical system (see Fig. 4). The wire grid diameter required in order to avoid vignetting of the beam is 130mm . The two output beams from WG_{IN} are fully polarized; both contain radiation from both input sources, and are processed by two symmetrical MPIs. In the next subsection we follow the radiation path propagating and interfering inside the two MPIs.

5.3. Interferometer section

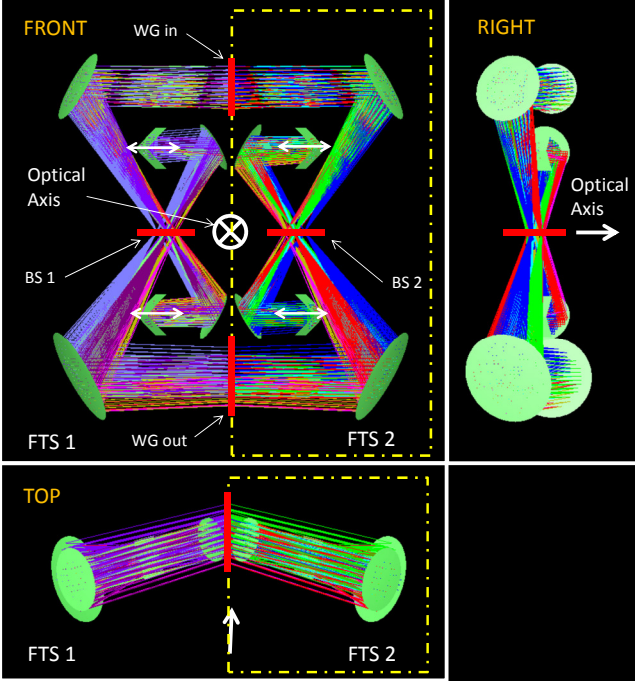


Fig. 7. Orthogonal views of the two MPIs. The optical axis of the Cassegrain telescope is marked for reference. The moving roof mirrors of the 4 delay lines are marked by double arrows.

The optical design of the MPIs is shown in Fig. 7. Undesired rotation of the polarization orientation is avoided by developing the two MPIs along two slant planes. These are tilted with respect to a plane normal to the telescope optical axis by $\pm 16^\circ$. As evident from Fig. 7, we also need to preserve a volume along the telescope optical axis for the folding mirror intercepting the telescope beam. This fact limits the available space for the delay lines, that have to be folded up to avoid vignetting.

The two MPIs are completely symmetric. The outgoing beam from WG_{IN} is collimated and directed towards the beam-splitter wire grid (BS) and the delay lines. Due to its divergency we need to use two additional aspheric collimators, minimizing the dimensions of the optical system and the aberrations, and limiting the effect of the retroreflector motion. A second biconic collimator ($Coll_{II}$) focuses radiation onto the BS; a parabolic collimator ($Coll_{RM}$) produces the parallel beam to illuminate the two roof mirrors (RM) retroreflectors of each MPI. The optimization performed allow us to limit the diameter of the BS wire grid to 50mm . The room available for the delay lines allows a 40mm mechanical travel for each RM. The opposite motions of the two RMs in the same MPI double the optical path difference, so that we reach a maximum spectral resolution 1.9 GHz per spectral element.

In the RMs the polarization axis of the incident beam is rotated by 90° , so that, after reflection on the RM, the beam which had been reflected by the BS is sent back to the BS, which will transmit it, while the beam which had been transmitted by the BS will be reflected. Both beams are directed towards the output polarizer (WG_{OUT}) by means of a third biconic collimator mirror ($Coll_{III}$). This has the same optical parameters as $Coll_{II}$, but has a wider size to avoid vignetting. Consequently WG_{OUT} has a diameter of 180mm . This last wire grid combines the power

from both the MPIs. With this configuration the power at the two output ports of the DFTS is close to 100% of the input power.

In the next subsection we'll describe the output section of the DFTS.

5.4. Output section

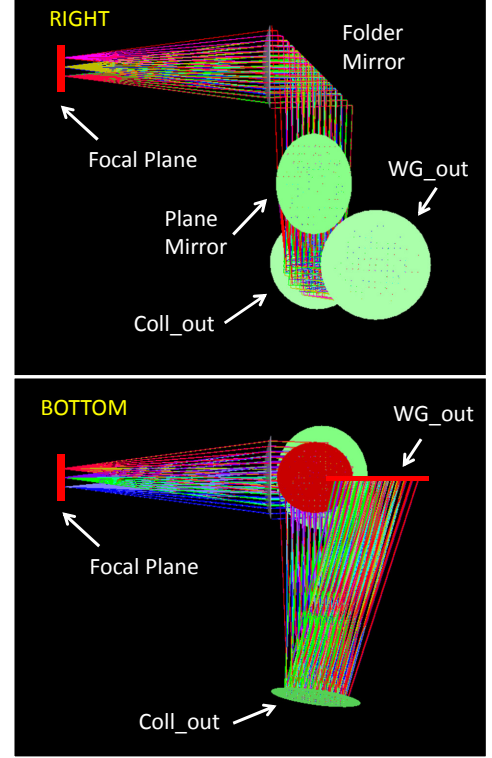


Fig. 8. The output section of the DFTS

The outputs of WG_{OUT} contains power from both input sources (the two halves of the sky field of view split by the wedge mirror) and from both the MPIs. Each of the two outputs contains 50% of the incident radiation collected by the telescope.

We use only one of the two output beams and we focus it to produce the original output focal ratio of the telescope ($f/3.3$). This is obtained by means of an aspherical mirror ($Coll_{OUT}$) and a flat mirror, redirecting the beam onto the rear face of the same 45° folding mirror we used to intercept the beam from the telescope (see Fig. 8). $Coll_{OUT}$ has a biconic profile with very large radii to optimize the final focalization of the beam. This is completed by a plano-convex lens (made of high density polyethylene) which corrects aberrations and reproduces the original focal ratio of the telescope.

5.5. Imaging performance

The DFTS was designed to have imaging capabilities. The FOV of the instrument is defined by the fraction of the focal plane covered by the wedge mirror at the entrance of the DFTS. Looking at Fig. 9 (right) we can compare the configuration of the input fields on the wedge mirror level to the configuration of the same fields on the detectors focal plane. The two center ray-traced fields come from the centers of the two faces of the wedge, and, after being processed by the DFTS, are focused in the center

of the detectors focal plane. The rectangular area represents the surface of the wedge and the colored spots are the field arranged in a pattern that covers a sky area of $0.22^\circ \times 0.11^\circ$. The image of the sky is split along the red dots line, and in the focal plane we have a differential spectral image, where each spot represents the difference between mirrored sky positions.

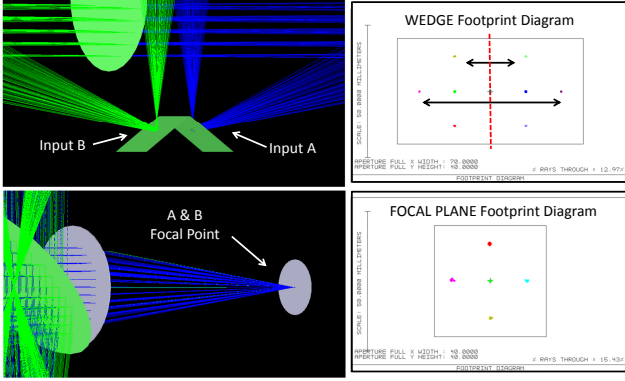


Fig. 9. Combination of pixel couples from the right half and the left half of the telescope focal plane (where the wedge mirror is located, top right diagram) into single pixels in the detectors focal plane (bottom right diagram). Images of the ray-tracing near the wedge mirror (top left) and near the detectors focal plane (bottom right) are also shown.

Our optical optimization preserves the initial optical quality, as evident from the spot diagrams in Fig. 10: both at the wedge mirror and at the final focal plane all the fields spots are well inside the Airy disc, for a frequency up of 600GHz .

5.6. A plug-in module

Our instrument has been designed as a plug-in optical processing module for the existing OLIMPO instrument. For this reason the optical elements assembly including the 45° folding flat mirror and the output lens can be inserted in or removed from the optical path between the telescope and the detectors cryostat. When the assembly is inserted, the front surface of the folding mirror reflects the beam coming from the telescope into the spectrometer, and its rear surface reflects the spectrometer-processed beam towards the lens and the detectors cryostat. When the assembly is removed, the spectrometer is excluded, and the OLIMPO instrument works as a 4-bands photometers array. The folding mirror / lens assembly is mounted on a trolley on rails (SKF model LWRM/V) which is moved orthogonally to the beam by a linear actuator, on command. The mechanical system provides a position repeatability of a few microns when inserting the folding mirror in the optical path.

5.7. Mechanical structure

The main problem in the mechanical design of a balloon-borne instrument is to create a light-weight structure stiff enough to maintain the alignment of the instrument despite of the orientation with respect to the gravity vector and the large temperature change ($\sim +30\text{C}$ on the ground, $\sim -40\text{C}$ at float). Our constraint was to keep the weight of the spectrometer below 3% of the total weight of the payload (i.e. 70 kg). Due to the throughput of the OLIMPO instrument, the necessary volume is large

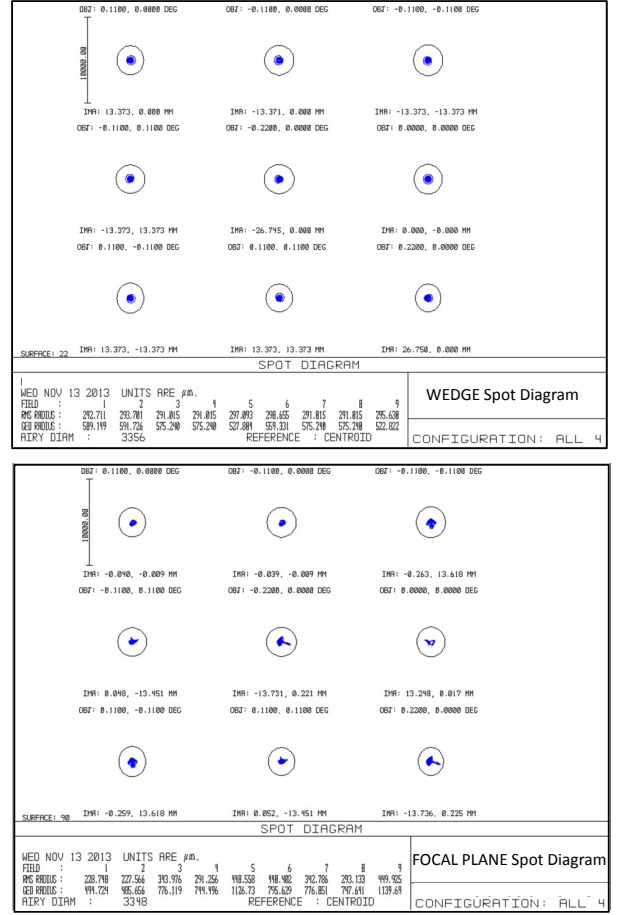


Fig. 10. Spot diagrams at the input and at the output of the DFTS. The dispersion of the points is due to the geometrical aberrations resulting from the sum of all the mirrors in the telescope (top panel) and in the DFTS (bottom panel). The circles represent the Airy disk at a frequency of 600GHz . The nine fields in each panel refer to positions in the sky covering a rectangular area of $26,4 \times 13,2$ arcminutes, that is the FOV of the instrument.

(of the order of 150 liters). The frame supporting all the optical elements can be up to 0.7 m in size in two dimensions, and needs to be squeezed to 0.3 m in the third dimension to fit the available room between the rear side of the primary mirror and the window of the detectors cryostat. We have used rectified Al alloy (Mic6) flanges to build the frame. In this way the frame and the mirrors share the same thermal expansion coefficients (0.0234mm/m/C). Even if this is about a factor 2 larger than that for a steel structure, it matches the thermal expansion of the telescope, whose structure and mirrors are made of Al alloys as well. All flanges are mounted together using M5 screws and pins. Careful finite elements analysis optimization results in a relatively light-weight frame (60 kg).

We exploit the symmetry properties of our design by mounting the four beamsplitters (WG_{IN} , WG_{OUT} , $WG_{BS,L}$, $WG_{BS,R}$) on two crossed flanges, and all the mirror support plates near the corners of the frame. The bottom flange (10 mm thick, with large sections reduced to 3 mm) is an optical bench, mounting the collimators supports and the delay lines on a side, and acts as the mechanical interface to the telescope frame on the other side. The top beams only contribute to the general stiffness of the frame, and support light-weight closure sheets. The frame includes rails and linear bearings to move the folding mirror in and

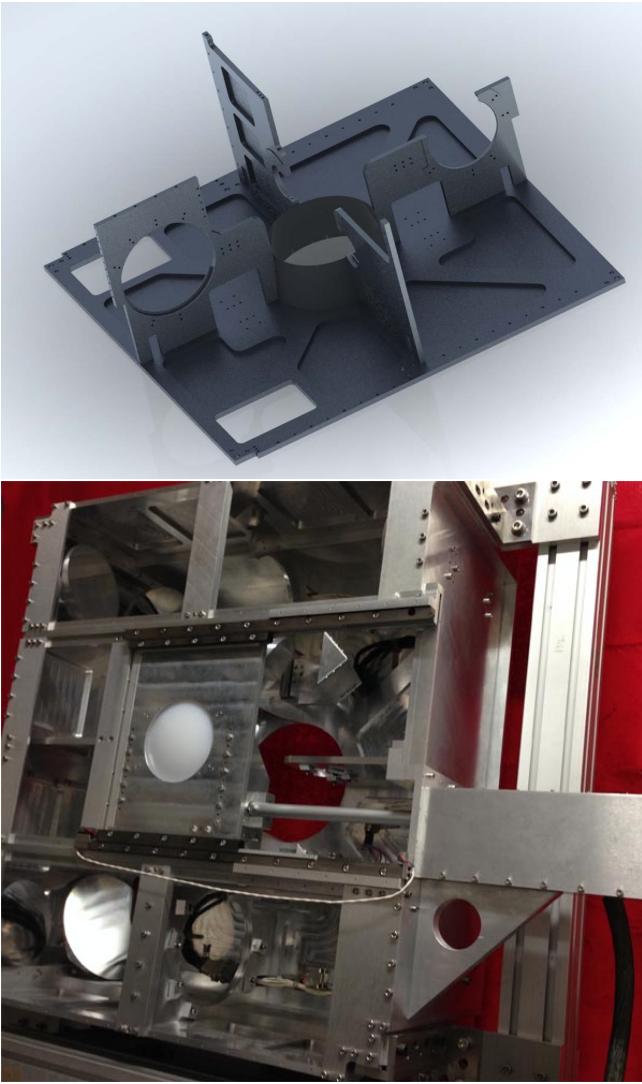


Fig. 11. Top: 3D drawing of the structure supporting the 4 polarizers of the instrument (WG_{IN} , WG_{OUT} , $WG_{BS,L}$, $WG_{BS,R}$). **Bottom:** Picture of the frame integrated with all the optical components. The volume of the main body is $70 \times 70 \times 33$ cm³. The protruding beam supports the linear motor moving the folding-flat / lens assembly, to exclude or include the MPI in the optical path of the OLIMPO instrument.

out of the OLIMPO optical path. All the frame parts were machined to H7 tolerance. The resulting frame is shown in Fig. 11. The maximum deflection of the loaded optical bench under the effect of gravity (any direction) is below 0.01mm over 70 cm. To avoid internal reflections and to reduce straylight, all the internal walls of the DFTS are covered with ECCOSORB[®]. Internal shields and the input hood further reduce the straylight level.

5.8. Delay lines and their fine tuning

The delay lines are the main active components in the FTS. The delay introduced must be controlled with high precision (see section 6) and should not introduce other biases in the measurement. In our optical configuration both arms of each interferometer have moving roof mirrors. One arm is shortened while the other is elongated by the same amount. In this way we double the optical path difference and the spectral resolution while keeping

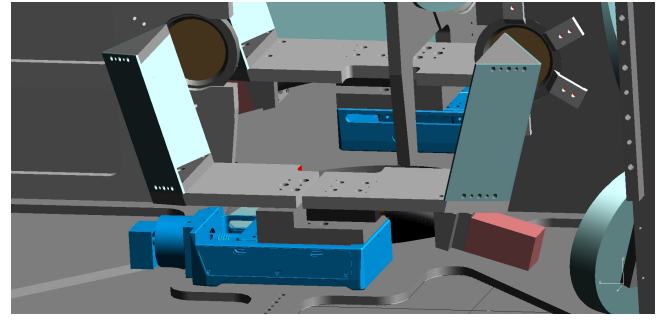


Fig. 12. 3D drawing of the delay lines assembly, showing the two roof mirrors (one for the left interferometer and one for the right interferometer), the linear stage PLS85 controlling the introduced delay (between the delay line assembly and the optical bench) and the tuning stage APT38 (below the right roof mirror).

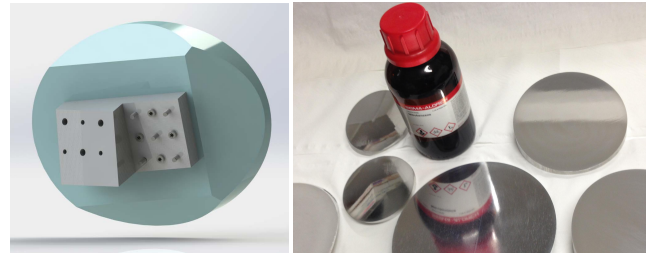


Fig. 13. Left: 3D drawing of the rear side of the collimators, showing the flat interface to the optical bench. **Right:** picture of the polished front surfaces.

constant the instrument size. The motion of the two linear stages of the same interferometer has to be synchronized so that exactly opposite delays are introduced. We have used two linear motion stages model PLS-85 from MICOS, adapted for vacuum and low-temperature operation. Each linear stage moves an assembly of two roof mirrors, one for each interferometer. The relative position of the two mirrors moved by the same stage can be tuned by means of an additional linear stage (APT38 from MICOS), which allows for fine adjustment of the distance between the two mirrors. In this way we can finely match the optical path differences introduced by the two interferometers. The resulting moving assemblies are visible in Fig. 12. With this arrangement, the delays in the two interferometers can be equalized to better than $0.5 \mu\text{m}$, as checked by maximizing the zero optical path difference peak in wide-band interferograms.

5.9. Collimator and roof mirrors

All mirrors were machined from Al alloys (AA2024 for the flat mirrors; AA6082T6 for the curved mirrors) using CAM milling, with 0.1 mm machining steps. These materials have been selected to optimize the quality of polishing and the thermal stability. The mirror surface has been obtained from a solid block including the bottom flat interface to the optical bench, as visible in Fig. 13. In ideal conditions, the flat surface matches the optical bench, with pins aligning the mirror in the nominal position. Would this positioning be modified for improved alignment, this is possible by removing the pins and using push screws. Hand polishing of the surface was obtained with a cloth using polishing pastes with diamond dust grains progressively smaller ($15 \mu\text{m}$, $9 \mu\text{m}$, $3 \mu\text{m}$, and $1 \mu\text{m}$). After each polishing step the mirror is ultrasonically cleaned in ethanol. The final polishing is

done using a small drill rotating a cloth dipped in $1\mu\text{m}$ diamond dust (see Fig. 13). The deviation from the ideal mirror profile, as measured using a Mitutoyo long stroke linear gage touch probe on a micrometric linear stage, is lower than $3\mu\text{m}$ rms for all mirrors.

5.10. Polarizers

We have used high efficiency wire-grid polarizers, made of parallel tungsten wires, $10\mu\text{m}$ in diameter, and spaced by $25\mu\text{m}$ for the WG_{BS} and $20\mu\text{m}$ for the WG_{IN} and WG_{OUT} , stretched across a steel support ring. This combination is well suitable for large temperature excursions (is used even in cryogenic systems). The polarizers where provided by QMC instruments, and feature an efficiency very close to 100% for both transmission and reflection, and a cross-polarization better than -40 dB . The correct positioning of the wire grids is achieved by means of support rings with mating pins, so that the orientation is precise to better than 0.1° .

6. Random errors and systematic effects

An important issue in FTS interferometry is the accuracy and the precision of the delay line motorized stages. In the case of a double MPI this issue can be critical, because the positioning and motion of the four roof mirrors has to be perfectly synchronous, to avoid loss of signal and distortions of the interferogram. For this system we can imagine two kinds of error: the first is due to random positioning errors of the roof mirrors with variance σ_x ; the second one is produced by a systematic mismatch of the delays of the two interferometers. Very precise, tunable and reproducible mechanical actuators are needed for the delay lines. The PLS-85 motorized linear stage provides 50mm of mechanical travel, and a nominal positioning precision of $< 1\mu\text{m}$ rms. The APT38 equalization stages provides a resolution better than $2\mu\text{m}$. In the following we describe the results of simulations computing the errors introduced in the spectra by non idealities in the delay lines.

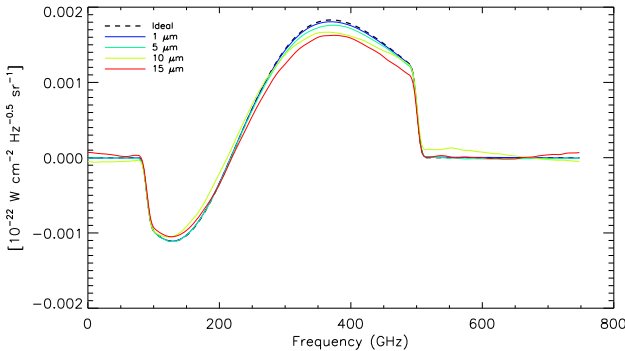


Fig. 14. Simulated spectra of the SZE estimated from interferograms with random positioning errors $\sigma_x = (1, 5, 10, 15)\mu\text{m}$. Only if $\sigma_x > 5\mu\text{m}$ there is a significant impact on the measurements. A smoothed-box window extending from 90 GHz to 500 GHz has been used in the analysis to remove frequencies which are not of interest here.

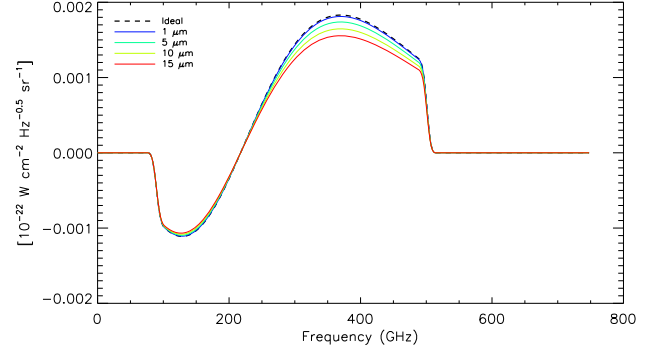


Fig. 15. Simulated spectra of the SZE estimated from interferograms with an error in the delay lines equalization of $(1, 5, 10, 15)\mu\text{m}$. Again, only if the equalization is off by $> 5\mu\text{m}$ there is a significant effect.

6.1. Random positioning errors

We have simulated interferograms measured during observations of a SZ spectrum, with random deviations from the nominal positions x_i . The deviations are gaussian distributed, with a standard deviation $\sigma_x = (1, 5, 10, 50)\mu\text{m}$. The simulated spectra, assuming a negligible contribution from the fluctuations of the common mode, are shown in Fig. 14. The PLS-85 motorized stages used in our interferometer have a positioning accuracy $\sigma_x < 1\mu\text{m}$ rms: from the results of the simulation it is evident that this does not degrade at all the quality of the measurements. We have also measured the total travel resulting from the sum of a large number of steps, to see if there is a measurable effect due to a possible miscalibration of the step size. For both stages the step size is accurate to 0.01%, so that will not affect our measurements.

6.2. Tuning of the delay lines lengths

The two interferometers should process radiation introducing exactly the same delay. For this reason, as explained in paragraph 5.8 we have added a tuning stage APT38 to match the delays in the two interferometers. A balloon-borne instrument changes its temperature by a significant amount, from say $+30\text{C}$ before launch and in the laboratory to $\sim -40\text{C}$ at float. The resulting change in all the dimensions of the FTS could produce a shift of the delay lines position with respect to the laboratory ones. For this reason the APT38 can be moved remotely, during the flight, by means of telemetry commands. We have performed a simulation to estimate the effect of a mismatch of the two delay lines of $(1, 5, 10, 15)\mu\text{m}$ for SZ observations as in paragraph 6.1. The results are in shown in Fig. 15. With 1-2 μm of mismatch, achievable with the APT38, the effect is a very slight deformation at the high-frequency end of the measured spectrum.

7. Tests and commissioning

7.1. Alignment

With all mirrors in their nominal positions, the wire grids have been replaced by semi-reflective optical glasses (3 mm thick), providing beamsplitting of visible light from an expanded laser placed at the input port of the spectrometer. A target crosswire is present in the optical glasses, so that collimators for each beamsplitter can be adjusted to center the laser beam. We are able to trace the whole optical path of the MPI checking the output po-

sitions of all the fields. The required mechanical adjustments were minimal, confirming the machining accuracy. After optical alignment, we started to measure interferograms of mm/submm sources.

7.2. Monochromatic measurements using a Gunn Diode

A 140 GHz Gunn diode with a power of a 20-30 mW has been used with a Golay cell room-temperature detector to measure the commissioning interferograms. The diode output is basically monochromatic (the first harmonic is down by a factor ~ 20 and we have used a low-pass filter with cut-off at 220 GHz to further reject the harmonics) and has been coupled to the interferometer using a single-mode feedhorn and two high-density polyethylene lenses, to match the input $f/\#$ of the DFTS. In Fig. 16 we present the interferogram obtained moving one roof mirror up to the maximum stroke of +2cm from the zero path difference (ZPD), and the other symmetrically to a maximum offset -2cm from the ZPD, producing a maximum optical path difference (OPD) of 8 cm, and spectra obtained for different maximum optical path differences. For the largest possible optical path difference introduced by our DFTS (8 cm) the width of the 140 GHz line is 1.87 GHz, consistent with the expectation $\Delta\sigma \sim 1/(2 \text{OPD}_{max})$ (the interferogram has been apodized with a triangular window). Decreasing the OPD the spectral resolution decreases as expected, while the signal to noise ratio for the measurement of continuum sources improves as $1/\Delta\sigma$.

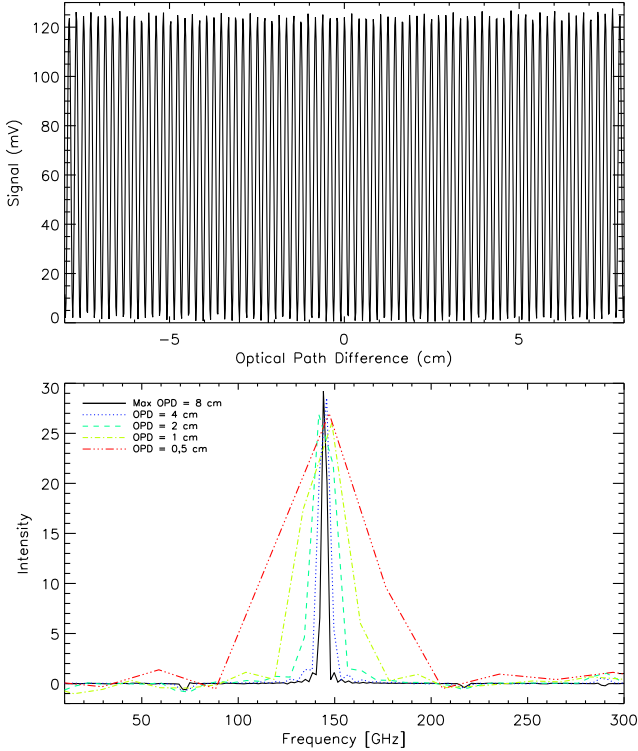


Fig. 16. Top: Interferogram measured with a D-band Gunn diode. **Bottom:** Spectra of Gunn diode emission obtained for different maximum optical path differences. Since the Gunn diode is effectively monochromatic, the measured widths represent direct measurements of the spectral resolution of the DFTS.

7.3. Continuum measurements

To test the performance at higher frequency, we have coupled the DFTS to a thermal source, a Hg lamp (Philips 125W) producing a $\sim 5000\text{K}$ grey body, and filtered the emission using different mesh filters. The source has been coupled to the interferometer by means of a two-lenses system, to reproduce the same $f/\#$ and beam of the OLIMPO telescope.

In Fig. 17 we plot the interferograms obtained through a 375 GHz bandpass filter, for two symmetric positions of the source, focusing radiation from the lamp in the centers of the two input ports of the DFTS (which are the centers of the two surfaces of the input wedge mirror). The two interferograms are highly symmetric, demonstrating the differential operation of the DFTS.

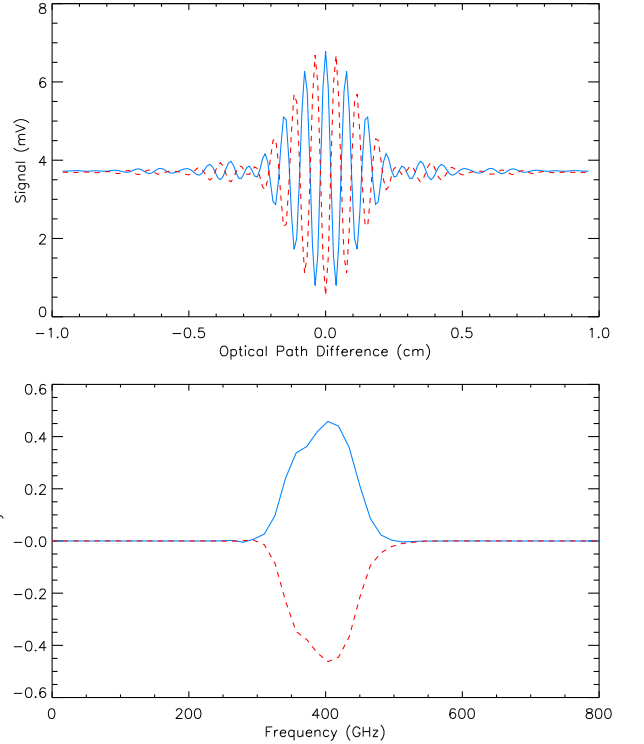


Fig. 17. Top: Interferograms measured with a Hg discharge lamp, band-pass filtered at 375 GHz, focusing at the centers of the two input ports of the DFTS. **Bottom:** Spectra obtained from the two interferograms above.

In Fig. 18 we compare the interferograms produced by each of the two FTSs present in the DFTS (each obtained by blanking the WG_{BS} of the other FTS) to the interferogram obtained from the simultaneous operation of the two FTSs. It is evident that the two FTSs are well aligned and contribute equally to the total signal. In this case a 600 GHz band-pass filter has been used to reduce the spectral width of the source. Even at this high frequency (basically the highest operative frequency of the instrument) the DFTS modulates efficiently the radiation under analysis.

7.4. Efficiency of the instrument

Our instrument can be bypassed to perform photometric measurements, as explained in section 5.6. When inserted, it reproduces at the output the same beamwidth and size of the input beam. We have compared the ZPD signal transmitted by our in-

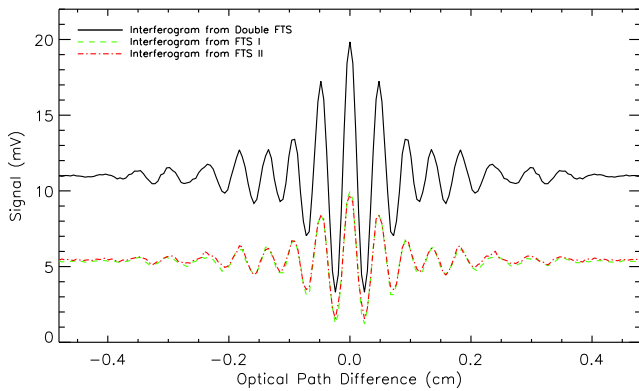


Fig. 18. Interferograms measured with a Hg discharge lamp, band-pass filtered at 600 GHz, for operation of the left FTS alone, of the right FTS alone, and of the complete DFTS. It is evident that the two FTSs are well aligned and contribute equally to the total signal. The DFTS is still modulating efficiently at this high frequency.

strument to the signal measured with the same detector when the spectrometer is bypassed, to assess the optical efficiency of the instrument. We find that for unpolarized sources the ratio between the two signals is $\gtrsim 90\%$ at 150 GHz, $\gtrsim 95\%$ at 220 GHz and 375 GHz, and $\gtrsim 80\%$ at 600 GHz.

In the spectroscopic configuration we have compared the height of the ZPD peak (above the baseline) to the baseline amplitude, to assess the interferometric modulation efficiency of the instrument. This is $\gtrsim 98\%$ at 145 GHz and $\gtrsim 80\%$ at 600 GHz.

8. Discussion and Conclusion

We have developed a Differential Fourier Transform Spectrometer optimized for low/medium resolution spectroscopy of faint brightness gradients. The instrument is efficient, features large throughput ($\sim 2.3 \text{ cm}^2 \text{ sr}$) and medium resolution ($\sim 1.9 \text{ GHz}$ FWHM, independent of frequency), in a relatively compact setup. The instrument is suitable for sub-orbital operation and will be tested in the forthcoming flight of the OLIMPO stratospheric balloon. A second implementation has been designed for operation in the W-band, at the Sardinia Radio Telescope. With a different mechanism for the mirror motion (see e.g. Schillaci *et al.* 2011 and references therein), the system can be implemented for operation in a cryogenic environment, suitable for space-based operation, as in the case of the SAGACE (de Bernardis *et al.* 2010) and Millimetron (Smirnov *et al.* 2012) missions.

Acknowledgements. This activity has been supported by MIUR PRIN 2009 "Mm and sub-mm spectroscopy for high resolution studies of primeval galaxies and clusters of galaxies" and by the contract OLIMPO of the Italian Space Agency. We thank Giorgio Amico and Stefano Banfi for carefully machining several parts of the instrument. We thank dr. Sebastiano Spinelli for implementing the procedure and test set-up for surface roughness and profile measurements on mirrors. We thank dr. Marco De Petris for help in interfacing the DFTS to laboratory sources. C. P. Novaes acknowledges the CNPq [237059/2012-6] fellowship.

References

Birkinshaw, M., *Physics Reports* 310, 97 (1999)
 Bock J.J., Parikh M.K., Fischer M.L., Lange A.E., *Appl Opt.* 34 4812-4816 (1995)
 Carli B., Mencaraglia F., *International Journal of Infrared and Millimeter Waves*, 2, 87-96 (1981)

Carli B., Mencaraglia F., *International Journal of Infrared and Millimeter Waves*, 2, 1045-1051 (1981)
 Carlstrom J. E., Holder G. P., Reese E. D., *Ann. Rev. Astron. and Astrophys.*, 40, 643-680 (2002)
 de Bernardis P., Bagliani D., A. Bardi, et al. "SAGACE: the Spectroscopic Active Galaxies And Clusters Explorer", proc. of the 12th Marcel Grossmann Meeting on General Relativity, Paris 12-18 July 2009; T. Damour, R. T. Jantzen, R. Ruffini eds., 2133, (2012), World Scientific, Singapore; astro-ph/1002.0867
 de Bernardis P. et al., *Astronomy and Astrophysics*, 538, A86 (2012)
 Fixsen D. J., Cheng E. S., Cottingham D. A., et al., *ApJ*, 420, 445-449 (1994)
 Griffin M. J., Abergel A., Abreu A., et al. *Astron. & Astrophys.*, 518, L3 (2010)
 Grueff G., Alvito G., Ambrosini R., et al. "Sardinia Radio Telescope: the new Italian project". *Proceedings of the SPIE (SPIE)* 5489, 773 (2004)
 Hasselfield M. et al., submitted to *J. Cosmology and Astroparticle Physics*, arXiv:1301.0816 (2013)
 Kompaneets A.S., *Soviet Phys. - JETP*, 4, 730 (1957)
 Martin D. and Puplett E., *Infrared Physics* 10, 105 109, (1970).
 Masi S., Ade P. A. R., de Bernardis P., et al. *Memorie della Societa Astronomica Italiana*, 74, 96, (2003)
 Mather J. C., Cheng E. S., Eplee Jr. R. E., et al., *ApJ.*, 354, L37-L40 (1990)
 Planck collaboration, "Planck 2013 results. XXIX. Planck catalogue of Sunyaev-Zeldovich sources", astro-ph/1303.5089 (2013)
 Rephaeli, Y., *Ann. Rev. Astron. and Astrophys.* 33, 541 (1995)
 Reichardt C. L., et al., *ApJ.*, 763, 127 (2013)
 Schillaci A. and de Bernardis P., *Infrared Physics*, 55, 40-44, (2011)
 Schillaci A. et al., *Infrared Physics & Technology*, 58, 64-68 (2013)
 Smirnov A. V., Baryshev A. M., Pilipenko S. V., et al., "Space mission Millimetron for terahertz astronomy", *Proc. SPIE 8442, Space Telescopes and Instrumentation 2012: Optical, Infrared, and Millimeter Wave*, 84424C (2012)
 Sunyaev, R.A., and Zel'dovich, Ya. B., *Comm. Astrophys. Space Phys.* 2, 66-74 (1970)
 Sunyaev, R.A., and Zel'dovich, Ya. B., *Comm. Astrophys. Space Phys.* 4, 173-178 (1970)
 Wright E. L., *ApJ.*, 232, 348 (1979)